

Boötes IV: A New Milky Way Satellite Discovered in the Subaru Hyper Suprime-Cam Survey and Implications for the Missing Satellite Problem

Daisuke Homma¹, Masashi Chiba², Yutaka Komiyama^{1,3},
Masayuki Tanaka¹, Sakurako Okamoto^{1,7}, Mikito Tanaka⁴,
Miho N. Ishigaki^{5,2}, Kohei Hayashi⁶, Nobuo Arimoto^{7,10}, Scott G. Carlsten⁸,
Robert H. Lupton⁸, Michael A. Strauss⁸, Satoshi Miyazaki^{1,3},
Gabriel Torrealba⁹, Shiang-Yu Wang⁹, and Hitoshi Murayama⁵

¹National Astronomical Observatory of Japan, 2-21-1 Osawa, Mitaka, Tokyo 181-8588, Japan

²Astronomical Institute, Tohoku University, Aoba-ku, Sendai 980-8578, Japan

³The Graduate University for Advanced Studies, Osawa 2-21-1, Mitaka, Tokyo 181-8588, Japan

⁴Department of Advanced Sciences, Faculty of Science and Engineering, Hosei University, 184-8584 Tokyo, Japan

⁵Kavli Institute for the Physics and Mathematics of the Universe (WPI), The University of Tokyo, Kashiwa, Chiba 277-8583, Japan

⁶ICRR, The University of Tokyo, Kashiwa, Chiba 277-8583, Japan

⁷Subaru Telescope, National Astronomical Observatory of Japan, 650 North A'ohoku Place, Hilo, HI 96720, USA

⁸Princeton University Observatory, Peyton Hall, Princeton, NJ 08544, USA

⁹Institute of Astronomy and Astrophysics, Academia Sinica, Taipei, 10617, Taiwan

¹⁰Astronomy Program, Department of Physics and Astronomy, Seoul National University, 599 Gwanak-ro, Gwanak-gu, Seoul, 151-742, Korea

*E-mail: chiba@astr.tohoku.ac.jp

Received (reception date); Accepted (acceptation date)

Abstract

We report on the discovery of a new Milky Way (MW) satellite in Boötes based on data from the on-going Hyper Suprime-Cam (HSC) Subaru Strategic Program (SSP). This satellite, named Boötes IV, is the third ultra-faint dwarf that we have discovered in the HSC-SSP. We have identified a statistically significant (32.3σ) overdensity of stars having characteristics of a metal-poor, old stellar population. The distance to this stellar system is $D_{\odot} = 209^{+20}_{-18}$ kpc with a V -band absolute magnitude of $M_V = -4.53^{+0.23}_{-0.21}$ mag. Boötes IV has a half-light radius of $r_h = 462^{+98}_{-84}$ pc and an ellipticity of $0.64^{+0.05}_{-0.05}$, which clearly suggests that this is a dwarf satellite galaxy. We also found another overdensity that appears to be a faint globular cluster with $M_V = -0.20^{+0.59}_{-0.83}$ mag and $r_h = 5.9^{+1.5}_{-1.3}$ pc located at $D_{\odot} = 46^{+4}_{-4}$ kpc. Adopting the recent prediction for the total population of satellites in a MW-sized halo by Newton et al. (2018), which combined the characteristics of the observed satellites by the Sloan Digital Sky Survey and the Dark Energy Survey with the subhalos obtained in Λ CDM models, we estimate that there should be about two MW satellites at $M_V \leq 0$ in the ~ 676 deg² covered by HSC-SSP, whereas that area includes six satellites (Sextans, Leo IV, Pegasus III, Cetus III, Virgo I and Boötes IV).

Thus, the observed number of satellites is larger than the theoretical prediction. On the face of it, we have a problem of too many satellites, instead of the well-known missing satellites problem whereby the Λ CDM theory overpredicts the number of satellites in a MW-sized halo. This may imply that the models need more refinements for the assignment of subhalos to satellites such as considering those found by the current deeper survey. Statistically more robust constraints on this issue will be brought by further surveys of HSC-SSP over the planned $\sim 1,400 \text{ deg}^2$ area.

Key words: galaxies: dwarf — galaxies: individual (Boötes IV) — globular clusters: individual (HSC 1) — Local Group

1 Introduction

The Λ -dominated cold dark matter (Λ CDM) model has become the standard cosmological model. A strong, immediate prediction of the model is that objects in the Universe grow hierarchically; they become progressively more massive with time through accretion and mergers. The Λ CDM model reproduces the observed cosmic large-scale structure on scales $\gtrsim 1 \text{ Mpc}$ extremely well (e.g., Tegmark et al. 2004). However, the model is not perfect, and there is extensive discussion in the literature of several persistent problems on smaller scales. These problems include the core or cusp problem (e.g., Moore et al. 1994; Burkert 1995; de Blok et al. 2001; Gilmore et al. 2007; Oh et al. 2011), the so-called too-big-to-fail problem (e.g., Boylan-Kolchin et al. 2011; Boylan-Kolchin et al. 2012, the satellite alignment problem (e.g., Kroupa et al. 2005; McConnachie & Irwin 2006; Ibata et al. 2013; Pawlowski et al. 2012; Pawlowski et al. 2013; Pawlowski et al. 2015), and the missing satellites problem (Klypin et al. 1999; Moore et al. 1999). The missing satellites problem, namely that a MW-sized halo is predicted to have significantly more subhalos than the observed number of dwarf satellites, simply refers to the satellite abundance, whereas the others are related to the internal density profiles of satellite galaxies and their dynamics in a MW-sized halo. It is thus important to fully understand the missing satellite problem in order to address the higher order issues.

A few possible solutions to the missing satellites problem have been proposed in the literature. One is to invoke baryon physics to suppress star formation in low-mass subhalos, thus making the majority of these low-mass halos starless (Sawala et al. 2016a; Sawala et al. 2016b). Another is to suggest that our catalogs of dwarf satellites is incomplete; we are not counting all the satellites due to observational constraints such as limited survey area and depth. These constraints may result in a significantly underestimated satellite abundance (Koposov et al. 2008; Tollerud et al. 2008). However, the observational situation has dramatically improved in recent years thanks largely to modern massive imaging surveys. The Sloan Digital Sky Survey (SDSS; York et al. 2000), the Dark Energy Survey (DES; Abbott et al. 2016), and the Pan-STARRS 1 (PS1) 3π

survey (Chambers et al. 2016) have covered wide areas of sky and discovered a large number of so-called ultra-faint dwarf galaxies (UFDs), whose V -band absolute magnitudes (M_V) are fainter than about -8 mag (e.g., Willman et al. 2005; Sakamoto & Hasegawa 2006; Belokurov et al. 2006; Laevens et al. 2014; Kim et al. 2015; Kim & Jerjen 2015; Laevens et al. 2015a; Laevens et al. 2015b; Bechtol et al. 2015; Koposov et al. 2015; Drlica-Wagner et al. 2015). Due to the relatively shallow depths of these surveys, however, UFDs at large distances are undetectable and the total count of dwarf galaxies around the Milky Way remains uncertain.

We are conducting an extensive search for UFDs using data from the Hyper Suprime-Cam Subaru Strategic Program (HSC-SSP) (Aihara et al. 2018a; Aihara et al. 2018b). HSC is a wide-field imager installed at the prime focus of the Subaru Telescope (Miyazaki et al. 2018), and a 300-night survey with this instrument is being carried out (Aihara et al. 2018a). The combination of the superb image quality ($\sim 0''.6$) and depth ($i \sim 26$) and the fact that it is a multi-band survey allows us to identify UFDs at large distances, filling in the parameter space unexplored by previous surveys. We have discovered two UFDs thus far, Virgo I and Cetus III, as reported in Homma et al. (2016) and Homma et al. (2018). The current paper presents the discovery of another UFD and a likely globular cluster from our continuing search.

The paper is structured as follows. Section 2 describes our search method, followed by detailed analyses of the identified stellar over-densities in Section 3. Section 4 discusses implications of our results for dark matter models, and Section 5 concludes the paper. Unless otherwise stated, magnitudes are given in the AB system.

2 Data and Method

We make use of the imaging survey data from the HSC-SSP Wide layer, which plans to cover $\sim 1,400 \text{ deg}^2$ over the northern sky in five, *grizy* photometric bands (Aihara et al. 2018a; Aihara et al. 2018b; Furusawa et al. 2018; Kawanomoto et al. 2018; Komiyama et al. 2018; Miyazaki et al. 2018). The

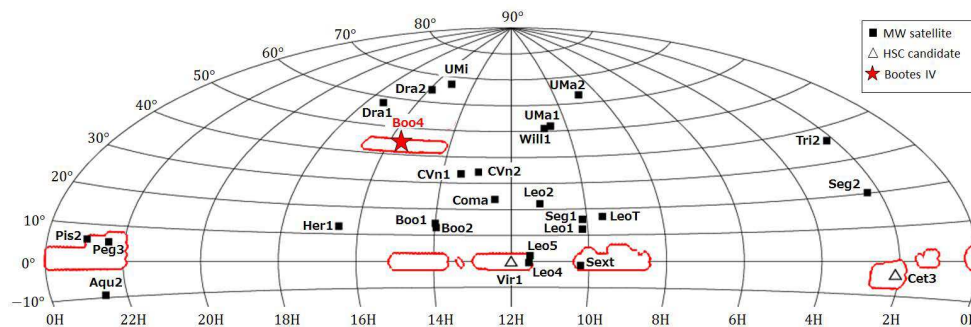


Fig. 1. Survey areas of the HSC-SSP for S18A (bounded by red curves). A red star denotes the location of the newly found satellite in this work, Boötes IV. Filled squares and empty triangles denote, respectively, the known satellites and those found in the HSC-SSP reported earlier. We note that Pis II and Leo V are just outside the HSC-SSP footprint.

target 5σ point-source limiting magnitudes in this Wide layer are given as $g = 26.5$, $r = 26.1$, $i = 25.9$, $z = 25.1$ and $y = 24.4$ mag. In this paper, we adopt the g , r , and i -band data obtained before 2018 April (internal data release S18A), which cover ~ 676 deg² in 6 separate fields along the celestial equator and one field around $(\alpha_{2000}, \delta_{2000}) = (242^\circ, 43^\circ)$ (Figure 1). This is to be compared with ~ 300 deg² covered in our previous searches of satellite galaxies from the data obtained before 2016 April (Homma et al. 2018). The HSC data have been processed using hscPipe v6.5 (Bosch et al. 2018), which is a branch of the Large Synoptic Survey Telescope (LSST) pipeline (see Ivezić et al. 2008; Axelrod et al. 2010; Jurić et al. 2017) calibrated against PS1 data of photometry and astrometry (e.g., Tonry et al. 2012; Schlafly et al. 2012; Magnier et al. 2013). These photometry data in HSC-SSP are corrected for the mean foreground extinction in the MW (Schlafly & Finkbeiner 2011).

2.1 Selection of stars

We use the same method to select target stars as in our previous work. In brief, we first select point-like images to avoid galaxies, set the criterion $g - r < 1$ to remove M-type main-sequence stars in the foreground, and then use the fiducial relation in the $g - r$ vs. $r - i$ diagram anticipated for stars to eliminate other contaminants.

In order to extract point sources from the data, we use the *extendedness* parameter calculated by the pipeline (Homma et al. 2018), which is defined on the basis of the ratio between PSF and cmodel fluxes (Abazajian et al. 2004), $f_{\text{PSF}}/f_{\text{cmodel}}$. A point source is defined to be an object with $f_{\text{PSF}}/f_{\text{cmodel}} > 0.985$. In what follows, we make use of this parameter measured in the i -band, where the typical seeing is the best of the five filters giving a median of $\sim 0''.6$. Aihara et al. (2018b) presented, by combining the data in HSC COSMOS with those in HST/ACS (Leauthaud et al. 2007), the definition for the completeness and contamination in the star/galaxy classification. The completeness is defined as the fraction of stars obtained

by ACS which are classified as stars correctly by HSC. This value is larger than 90% at $i < 22.5$, and decreases to $\sim 50\%$ at $i = 24.5$. The contamination is defined as the fraction of stars in the HSC classification which are actually galaxies in ACS. This value is nearly zero at $i < 23$ and increases to $\sim 50\%$ at $i = 24.5$. Here, we select stars as point sources down to $i = 24.5$.

Next, we adopt the criteria for colors to remove the other objects such as disk stars, background quasars and distant galaxies. These contaminants remained even after the *extendedness* cut. We use the $g - r$ vs. $r - i$ color-color diagram for stars with *extendedness* = 0 and galaxies with *extendedness* = 1 in the field called WIDE12H, where the bright limit of $i < 21$ mag is satisfied so that the star/galaxy classification is robust. Unlike galaxies, the distribution of stars in this color-color diagram follows a narrow sequence (see Figure 1 of Homma et al. (2018)). Thus, following previous works (e.g., Willman et al. 2002), we select stars located inside this sequence, after removing red stars (dominated by M-type dwarfs in the disk component) having a $g - r$ color of $g - r \geq 1$. This star sequence is characterized by a polygon bounded by $(g - r, r - i)$ of (1.00, 0.27), (1.00, 0.57), $(-0.4, -0.55)$, and $(-0.4, -0.25)$. This color cut has a width of $\Delta(r - i) = 0.3$ mag, which is wider than twice the typical 1σ photometric error of $r - i$ at $i = 24.5$. Thus, this method is optimal to select candidate halo stars in the MW.

2.2 Algorithm for the detection of the stellar overdensities

Dwarf satellites in the MW are characterized as metal-poor, old stellar systems, and they will present as statistically significant overdensities of stars compared to the random distribution of MW field stars and distant galaxies/quasars. We look for overdensities using the color-magnitude (CMD) isochrone-based matched filter summarized below (Homma et al. 2016; Homma et al. 2018) following the approach of Koposov et al. (2008) and Walsh et al. (2009).

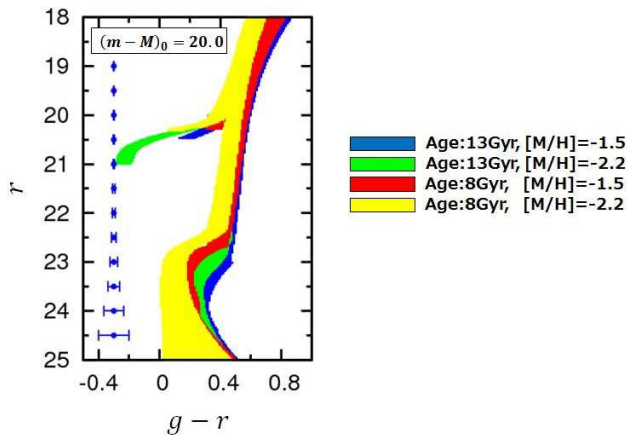


Fig. 2. CMD filters at a distance modulus of $(m - M)_0 = 20$ mag defined with an age of $t = 13$ Gyr and metallicity of $[M/H] = -1.5$ (blue area), $t = 13$ Gyr and $[M/H] = -2.2$ (green area), $t = 8$ Gyr and $[M/H] = -1.5$ (red area), and $t = 8$ Gyr and $[M/H] = -2.2$ (yellow area). The error bars correspond to the typical error in the measurement of color at each r -band magnitude.

2.2.1 Isochrone filters

The UFDs in the MW, that have been identified to date, show a similar distribution in the CMD diagram to MW globular clusters, i.e., a characteristic locus expected for metal-poor, old stellar systems. Following our previous work, we thus select stars located inside a CMD locus for a metal-poor, old stellar system within a specified distance interval from the Sun. This is a so-called isochrone filter, for which we use a PARSEC isochrone (Bressan et al. 2012) to define four different models: (a) an age of $t = 13$ Gyr and metallicity of $[M/H] = -1.5$, (b) $t = 13$ Gyr and $[M/H] = -2.2$, (c) $t = 8$ Gyr and $[M/H] = -1.5$, and (d) $t = 8$ Gyr and $[M/H] = -2.2$.

As a CMD, we use the $g - r$ color and r -band absolute magnitude, M_r . In order to work with the current HSC filter system (Kawanomoto et al. 2018), the SDSS filter system, which is available for the PARSEC isochrone, has been adopted and converted, as given in the Homma et al. (2016) paper. The finite selection width for the use of this isochrone filter is given as a function of r -band magnitude. We adopt the quadrature sum of a 1σ error in the measurement of the $(g - r)$ color in HSC imaging and a color dispersion being typically $\sim \pm 0.05$ mag expected for red giant-branch stars (RGBs) associated with a metallicity dispersion of typically $\sim \pm 0.5$ dex as seen in MW dSphs. This isochrone filter is shifted over distance moduli of $(m - M)_0 = 16.5 - 24.0$ in steps of 0.5 mag, to search for metal-poor, old stellar systems at heliocentric distances of $D_\odot = 20 - 631$ kpc. In Figure 2, we show our four isochrone filters placed at $(m - M)_0 = 20.0$.

2.2.2 Method to identify overdensities and estimate their statistical significance

Based on the isochrone filters at each distance from the Sun, we search for spatial overdensities and estimate their statistical significance. The stars selected in $0^\circ.05 \times 0^\circ.05$ boxes in right ascension and declination are counted, where an overlap of $0^\circ.025$ in each direction is adopted. We note that the grid interval of $0^\circ.05$ in this search is comparable to a half-light diameter of ~ 80 pc for a typical UFD at $D_\odot = 90$ kpc and that dwarf satellites located at or beyond this characteristic distance, which are our targets in HSC-SSP, can be identified within this grid interval.

In this procedure, we estimate the number of stars in each cell, $n_{i,j}$. We ignore cells without any stars, $n_{i,j} = 0$, which are for instance caused by masking near a bright-star image. Then, for each of the separate Wide-layer fields, we obtain the mean density (\bar{n}) and its dispersion (σ) over all cells and examine the normalized signal in each cell, $S_{i,j}$, which is the number of standard deviations relative to the local mean (Koposov et al. 2008; Walsh et al. 2009),

$$S_{i,j} = \frac{n_{i,j} - \bar{n}}{\sigma}. \quad (1)$$

The distribution of S is found to be almost Gaussian as obtained in our previous papers.

For the selection of candidate overdensities that have statistically high significance so that false detections are removed, we set the detection threshold, S_{th} , for the value of S (Walsh et al. 2009), following the result of a Monte Carlo analysis in our previous work (Homma et al. 2018). The characteristic distribution of S expected for purely random fluctuations in stellar densities is obtained and we estimate S_{th} from a maximum density contrast found as a function of \bar{n} . We adopt a threshold in the density contrast of $1.5 \times S_{\text{th}}$ to identify statistically significant overdensities, while avoiding contamination from random fluctuations.

3 Results

Using the algorithm above, we have detected two new overdensities beyond the above detection threshold, in addition to the previously discovered UFDs in the survey footprint. The first high signal is found at $(\alpha_{2000}, \delta_{2000}) = (15^{\text{h}}34^{\text{m}}45^{\text{s}}.36, +43^\circ43'33''.6)$ in the direction of Boötes ($S = 32.3$ with $\bar{n} = 1.48$, $S/S_{\text{th}} = 4.09$) and the second one is found at $(\alpha_{2000}, \delta_{2000}) = (22^{\text{h}}17^{\text{m}}14^{\text{s}}.16, +03^\circ28'48''.0)$ ($S = 31.8$ with $\bar{n} = 1.60$, $S/S_{\text{th}} = 4.20$). As explained below, the former is a dwarf galaxy candidate, hereafter called Boötes IV, and the latter appears to be a compact globular cluster, hereafter called HSC 1.

3.1 HSC J1534 + 4343 - a new satellite, Boötes IV

This high-density stellar system is found through the isochrone filter of $t = 13$ Gyr and $[M/H] = -2.2$ placed at $(m - M)_0 = 21.6$ mag. The left panel of Figure 3 depicts this system, in which stars are inside the isochrone filter at this distance modulus. The right panel corresponds to galaxies, which do not show any overdensity.

In Figure 4(a), we plot the spatial distribution of the objects classified as stars around the overdensity. There is a high-density region of stars within an ellipse with a major axis of $r = 2r_h$ ($r_h = 7'.6$) and an ellipticity of 0.64, where these values are obtained in Section 3.1.1. Figure 4(b) shows the CMD defined with $(g - r, r)$ for the stars within the ellipse given in panel (a). We identify a clear RGB locus, whereas this feature is absent for the stars in the annulus with $25'.0 < r < 26'.6$ which has the same solid angle, as shown in Figure 4(c). These are probably field stars outside the overdensity.

3.1.1 Structural parameters

Using a likelihood analysis, we calculate the heliocentric distance to this stellar system, for which we use RGB and blue horizontal-branch (BHB) stars inside the isochrone filter shown in Figure 4(b) obtained at the best-fit distance modulus of $(m - M)_0 = 21.6$ when we search for the overdensity. If we assume a Gaussian distribution for the probability of the photometry of these member stars relative to the best-fit CMD isochrone, we estimate a best distance modulus of $(m - M)_0 = 21.6^{+0.2}_{-0.2}$, corresponding to a heliocentric distance of $D_\odot = 209^{+20}_{-18}$ kpc.

As an alternative distance estimate, we identify the five blue horizontal-branch (BHB) stars in the range of $22.0 < r < 22.5$ and $-0.3 < g - r < 0$ (red circles in Figure 4(b)) and use these BHBs to determine the distance following the formula for their absolute magnitude calibrated by Deason et al. (2011). The detailed description for this method is given in Fukushima et al. (2019). We find that this procedure provides $(m - M)_0 = 21.59^{+0.14}_{-0.14}$, taking into account the typical photometric error in $g - r$ (0.02 mag) for the r magnitude of these BHBs. Since this estimate is consistent with the above distance estimate using the isochrone filter, we adopt $(m - M)_0 = 21.6^{+0.2}_{-0.2}$ in what follows.

Following Martin et al. (2008) and Martin et al. (2016), we obtain the structural properties of this overdensity. We define six parameters $(\alpha_0, \delta_0, \theta, \epsilon, r_h, N_*)$, where each of the parameters denotes the following meaning. (α_0, δ_0) denote the celestial coordinates for the center of the overdensity, θ is its position angle from North to East, ϵ is the ellipticity, r_h is the half-light radius measured on the major axis, and N_* is the number of stars within the isochrone and brighter than our magnitude limit, which belong to the overdensity. We then perform the maximum likelihood analysis given in Martin et al. (2008) for the stars within a circle of radius $30'$, corresponding to ~ 3.9

Table 1. Properties of Boötes IV

Parameter ^a	Value
Coordinates (J2000)	233° .689, 43° .726
Galactic Coordinates (l, b)	70° .682, 53° .305
Position angle	$+3^{+4}_{-4}$ deg
Ellipticity	$0.64^{+0.05}_{-0.05}$
Number of stars, N_*	124^{+10}_{-10}
Extinction, A_V	0.067 mag
$(m - M)_0$	$21.6^{+0.2}_{-0.2}$ mag
Heliocentric distance	209^{+20}_{-18} kpc
Half light radius, r_h	$7'.6^{+0'.8}_{-0'.8}$ or 462^{+98}_{-84} pc
$M_{\text{tot},V}$	$-4.53^{+0.23}_{-0.21}$ mag

^aIntegrated magnitudes are corrected for the mean Galactic foreground extinction, A_V (Schlafly & Finkbeiner 2011).

times the derived r_h , which pass the above isochrone filter. We summarize the results in Table 1.

We show, in Figure 5, the radial distribution of the stars passing the isochrone filter depicted in Figure 4(b), which is obtained from the count of the average density within elliptical annuli. The red line in the figure denotes the best-fit exponential profile having $r_h = 7'.6$ or 462 pc. We note that this spatial size is quite large compared with the typical scale of MW globular clusters, but is in agreement with that of MW dwarf galaxies, as we describe in Section 4.3.

3.1.2 V-band absolute magnitude

Here we estimate M_V of Boötes IV in the following manner. We first transform (g, r) to V using the formula given in Jordi et al. (2006), which are calibrated for metal-poor, Population II stars. We then perform a Monte Carlo procedure similar to Martin et al. (2008) for the estimation of the most likely value of M_V and its uncertainty. Using the values of $N_* = 124^{+10}_{-10}$ at $i < 24.5$ mag and $(m - M)_0 = 21.6^{+0.2}_{-0.2}$ mag as obtained in the procedure of Section 3.1.1 as well as a model for the stellar population having an age of 13 Gyr and metallicity of $[M/H] = -2.2$, the 10^4 realizations of CMDs are generated for the initial mass function (IMF) given by Kroupa (2002). The luminosity of the stars at $i < 24.5$ mag is then derived, also considering the completeness of the stars observed with HSC. We obtain the median value and the 68% confidence interval of M_V as $M_V = -4.53^{+0.23}_{-0.21}$ mag. These values are very insensitive to whether we choose the Salpeter (Salpeter 1955) or Chabrier IMF (Chabrier 2001). The total mass of stars in Boötes IV is also estimated for different IMFs, as $M_* = 14430^{+3350}_{-3939} M_\odot$ (Kroupa), $13779^{+3161}_{-3693} M_\odot$ (Chabrier), and $27730^{+6477}_{-7732} M_\odot$ (Salpeter).

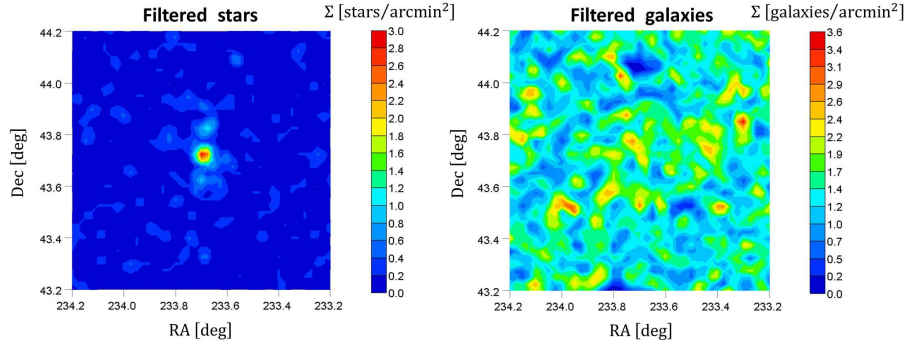


Fig. 3. Left panel: the stellar overdensity found in Boötes passing the isochrone filter of $t = 13$ Gyr and $[M/H] = -2.2$ at $(m - M)_0 = 21.6$ for the point sources satisfying $i < 24.5$, $g - r < 1.0$, and the color-color cuts expected for stars in the $g - r$ vs. $r - i$ diagram (see subsection 2.1) The plot is shown over 1 deg^2 centered on this UFD candidate. Right panel: the spatial distribution of the galaxies which pass the same isochrone filter and constraints as for the stars. No overdensity is found in this plot.

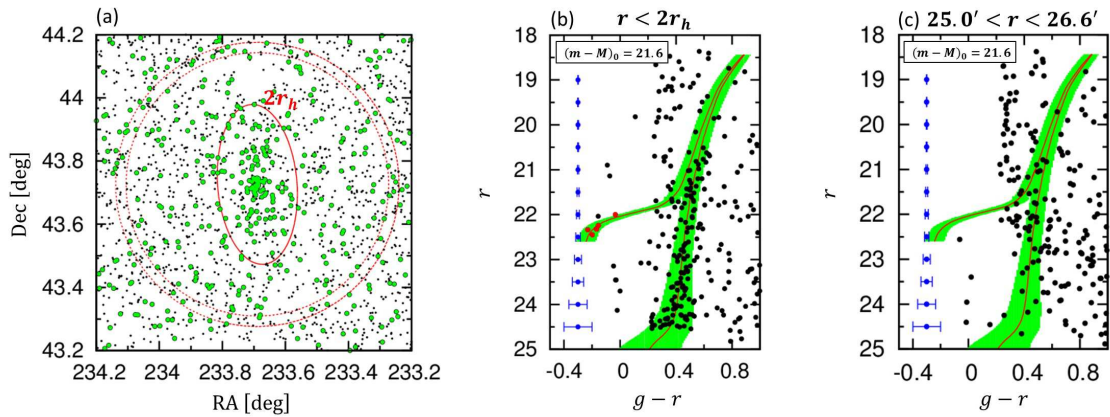


Fig. 4. (a) The spatial distribution of the objects classified as stars around the overdensity in Boötes. The green circles and black dots denote, respectively, the stars inside and outside the isochrone filter at the distance modulus of $(m - M)_0 = 21.6$. A solid red curve shows an ellipse with a major axis of $r = 2r_h$ ($r_h = 7'.6$) and an ellipticity of 0.64, whereas dashed red circles show annuli with radii $25'.0$ and $26'.6$ from the center of the overdensity. (b) The CMD of the stars defined as the $g - r$ vs. r relation, which are located within the solid red ellipse in panel (a). Red circles denote the five BHB stars for the use of the additional distance estimate as described in the text. (c) The same as (b) but for field stars at $25'.0 < r < 26'.6$ having the same solid angle. A red giant-branch feature is absent in this plot.

3.2 HSC J2217 + 0328 - a compact star cluster candidate, HSC 1

We have detected this overdensity having $S/S_{\text{th}} = 4.20$ and $\bar{n} = 1.60$ (31.8σ) is found with the isochrone filter of $t = 13$ Gyr and $[M/H] = -2.2$ placed at $(\alpha_{2000}, \delta_{2000}) = (334^\circ.309, 3^\circ.480)$ and $(m - M)_0 = 18.3$ mag. We show, in Figure 6, this overdensity passing the isochrone filter at this distance for the objects classified as stars (left) and galaxies (right). While there is a clear overdensity signal in stars, we also identify an overdensity in galaxies at the same position. We suggest that this is caused by the misclassification of faint stars within a cluster as galaxies in hscPipe. To get insights into this overdensity feature, we plot the gri color map of the HSC image around its location in Figure 7. One can see the concentration of point sources directly by eye. This overdensity is a candidate star cluster, which is hereafter called HSC 1 because it is the first new cluster found

with HSC.

As mentioned above, hscPipe has misclassified some stars as galaxies within the cluster, which may be due to the deblender failure of this crowded region and the resultant failure of the star/galaxy separation. To mitigate this effect, we use the un-deblended flux of the HSC image with a seeing-matched aperture magnitude to select likely member objects belonging to this overdensity. In Figure 8(a), we plot the spatial distribution of all objects after color cuts around this overdensity, both those classified as stars and galaxies. There is a localized concentration of objects within an ellipse with a semi-major axis of $r_h = 0'.44$ and an ellipticity of 0.46. Figure 8(b) shows the CMD defined with $(g - r, r)$ for objects within the solid red ellipse shown in panel (a). We have found a clear signature of a main sequence (MS), whereas there is no such feature for the objects at $2'.0 < r < 2'.1$ having the same solid angle, as shown in Figure

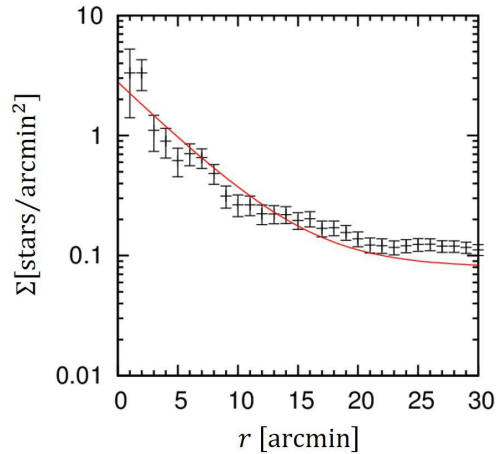


Fig. 5. The density distribution of the stars in Boötes IV passing the isochrone filter given in Figure 4(b), in elliptical annuli as a function of mean radius. The uncertainties are based on Poisson statistics. The red line denotes the best-fit exponential profile with $r_h = 7'.6$, plus a constant representing the background.

8(c). These are probably field stars outside the overdensity.

In the same way as for Boötes IV, we estimate heliocentric distance, structural parameters and V-band absolute magnitude for this stellar system as follows. We adopt PSF magnitudes for these estimates.

Based on a likelihood analysis, we estimate the D_\odot to this stellar system, for which we use MS stars inside the isochrone filter shown in Figure 8(b) obtained at the best-fit distance modulus of $(m - M)_0 = 18.3$ when we search for the overdensity. We obtain a best distance of $(m - M)_0 = 18.3^{+0.2}_{-0.2}$, corresponding to a heliocentric distance of $D_\odot = 46^{+4}_{-4}$ kpc.

The structural properties of this stellar system are derived by applying the maximum likelihood method to the objects (Martin et al. 2008) located within a circle of radius $3'.0$ passing the isochrone filter, which corresponds to ~ 6.8 times the anticipated r_h . We note that this method models the contribution for the background uniformly distributed objects like galaxies, and therefore is applicable to the structural analysis of the star cluster even though we have not filtered out the galaxies. The results are summarized in Table 2.

Figure 9 shows the radial density distribution of the stars passing the isochrone filter, which is obtained from the count of the average density within elliptical annuli. The red line denotes the best-fit exponential profile having $r_h = 0'.44$ or 5.9 pc.

The M_V of this stellar system is estimated in the same way as for Boötes IV and we obtain $M_V = -0.20^{+0.59}_{-0.83}$ mag. We also calculate the total mass of stars in HSC 1 for different IMFs as $M_* = 254^{+58}_{-51} M_\odot$ (Kroupa), $255^{+55}_{-51} M_\odot$ (Chabrier), and $487^{+111}_{-99} M_\odot$ (Salpeter). The combination of the absolute magnitude and small half-light radius suggests that HSC 1 is a compact star cluster as will be discussed in Section 4.1. That

Table 2. Properties of a star cluster candidate, HSC 1

Parameter ^a	Value
Coordinates (J2000)	$334^\circ.309, 3^\circ.480$
Galactic Coordinates (l, b)	$66^\circ.319, -41^\circ.841$
Position angle	-12^{+11}_{-11} deg
Ellipticity	$0.46^{+0.08}_{-0.10}$
Number of stars, N_*	47^{+6}_{-6}
Extinction, A_V	0.222 mag
$(m - M)_0$	$18.3^{+0.2}_{-0.2}$ mag
Heliocentric distance	46^{+4}_{-4} kpc
Half light radius, r_h	$0'.44^{+0'.07}_{-0'.06}$ or $5.9^{+1.5}_{-1.3}$ pc
$M_{\text{tot},V}$	$-0.20^{+0.59}_{-0.83}$ mag

^a Integrated magnitudes are corrected for the mean Galactic foreground extinction, A_V (Schlafly & Finkbeiner 2011).

is, this is a MW globular cluster as judged from its location far beyond the MW disk. However, to really distinguish between star clusters and galaxies, we need to determine if this object is embedded in a dark matter halo, which will require measuring accurate stellar radial velocities.

4 Discussion

4.1 Comparison with MW globular clusters and dwarf galaxies

We first compare the structural properties of Boötes IV and HSC 1 with those of previously known MW globular clusters and dwarf satellites. Globular clusters are characterized by their compact size and round shape without having a surrounding dark halo, suggesting a self-gravitating stellar system. On the other hand, dwarf satellites have an extended spatial distribution of stars, and their velocity distribution strongly suggests the presence of a surrounding dark halo.

Figure 10(a) shows the relation between the half-light radii and absolute magnitudes of globular clusters in the MW (dots) (Harris 1996) and those of dwarf satellites (squares) (McConnachie 2012; Laevens et al. 2014; Bechtol et al. 2015; Koposov et al. 2015; Drlica-Wagner et al. 2015; Kim et al. 2015; Kim & Jerjen 2015; Laevens et al. 2015a; Laevens et al. 2015b; Torrealba et al. 2016; Torrealba et al. 2018). Red and blue stars with error bars, respectively, denote Boötes IV and HSC 1. It is clear that Boötes IV is significantly large compared with MW globular clusters having similar M_V and that it follows the locus of MW dwarf satellites. This suggests that Boötes IV is a typical UFD, whose shape is flattened with an ellipticity of $\epsilon = 0.64^{+0.05}_{-0.05}$. Globular clusters have much smaller ellipticities at its brightness (Harris 1996; Marchi-Lasch et al. 2019), while some dwarf galaxies have even larger ellipticities, e.g., UMa I having $\epsilon = 0.80$ (Martin et al. 2008), supporting this conclusion. On the other hand, the size of HSC 1 is comparable to MW globular clusters. This suggests that HSC 1 is a globular cluster, although it is still possible that it is a compact

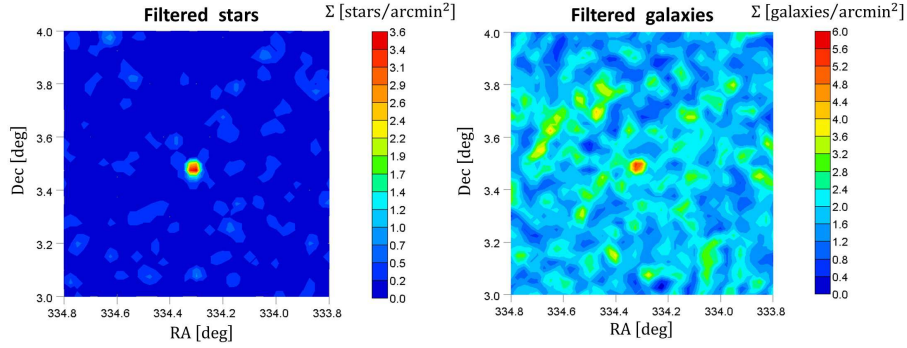


Fig. 6. Left panel: the stellar overdensity found in the vicinity of a star cluster candidate, HSC 1, passing the isochrone filter of $t = 13$ Gyr and $[M/H] = -2.2$ at $(m - M)_0 = 18.3$ for the point sources satisfying $i < 24.5$, $g - r < 1.0$, and the color-color cuts expected for stars in the $g - r$ vs. $r - i$ diagram (see subsection 2.1). The plot is shown over 1 deg^2 centered on this star cluster candidate. Right panel: the spatial distribution of the galaxies which pass the same isochrone filter and constraints as for the stars. An overdensity at the center of this plot is seen, possibly because of misclassification of faint stars within a cluster as galaxies in hscPipe.

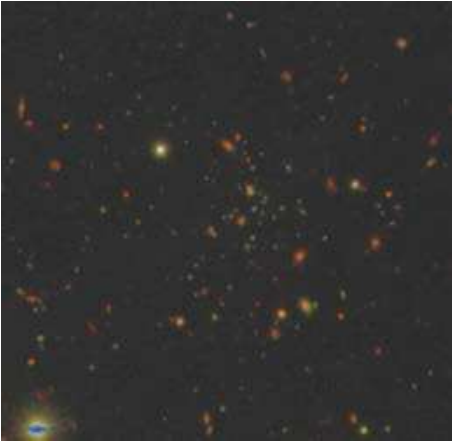


Fig. 7. The gri color map of the HSC image within a $2' \times 2'$ box around the overdensity, HSC 1.

dwarf galaxy because HSC 1 lies on the M_V vs. r_h relation for dwarf galaxies and its ellipticity, $\epsilon = 0.46$, at $M_V = -0.20$ mag is typical for both dwarf galaxies and globular clusters at such faint magnitudes (Marchi-Lasch et al. 2019).

4.2 Detectability of Boötes IV and HSC 1 in other surveys

The footprint of HSC-SSP overlaps that of SDSS, so we investigate the detectability of Boötes IV and HSC 1 in both surveys. For this purpose, we evaluate the completeness distance, $R_{\text{comp}}^{\text{SDSS}}$, derived for SDSS, above which a satellite with a particular luminosity is undetectable, and the corresponding distance for HSC-SSP, $R_{\text{comp}}^{\text{HSC}}$. Following Koposov et al. (2008), the former is given as,

$$R_{\text{comp}}^{\text{SDSS}} = 10^{(-a^* M_V - b^*)} \text{ Mpc}, \quad (2)$$

where $(a^*, b^*) = (0.205, 1.72)$. $R_{\text{comp}}^{\text{HSC}}$ is then given as (Tollerud

et al. 2008),

$$R_{\text{comp}}^{\text{HSC}} / R_{\text{comp}}^{\text{SDSS}} = 10^{(M_{r,\text{HSC}} - M_{r,\text{SDSS}}) / 5}, \quad (3)$$

where $M_{r,\text{HSC}}$ and $M_{r,\text{SDSS}}$ are, respectively, the limiting point-source magnitudes in r -band for HSC and SDSS. In this paper, we adopt $M_{r,\text{SDSS}} = 22.2$ mag at $\sim 100\%$ completeness and $M_{r,\text{HSC}} = 24.7$ mag at $\sim 50\%$ completeness, because the cut-off i -band magnitude adopted in this work is set as $i = 24.5$ mag and the stars in MW satellites typically have $r - i = 0.2$.

Figure 10(b) presents the M_V vs. D_\odot relation for MW globular clusters and dwarf galaxies including Boötes IV and HSC 1. Red and blue lines show, respectively, the detection limits of SDSS and HSC evaluated from equations (2) and (3). As is clear, both Boötes IV and HSC 1 are beyond the reach of SDSS but (not surprisingly) within the limit of HSC.

4.3 Implication for dark matter models

We have discovered one new dwarf satellite, Boötes IV, from the HSC-SSP data released internally in the outer halo of the MW, in addition to two satellites, Virgo I and Cetus III, which we discovered in the previous data release (Homma et al. 2016; Homma et al. 2018). To compare this discovery rate with the prediction of Λ CDM models, we adopt the recent study of Newton et al. (2018) for the number of visible satellites expected in Λ CDM models.

Newton et al. (2018) combined the data from SDSS and DES to infer the full complement of MW satellite galaxies. For this purpose, they adopted the subhalo populations for MW-sized halos performed by the simulation project, AQUARIUS (Springel et al. 2008), to obtain a prior for the radial distribution of satellites. They made use of dark-matter-only simulations for six MW-sized halos and considered two effects that

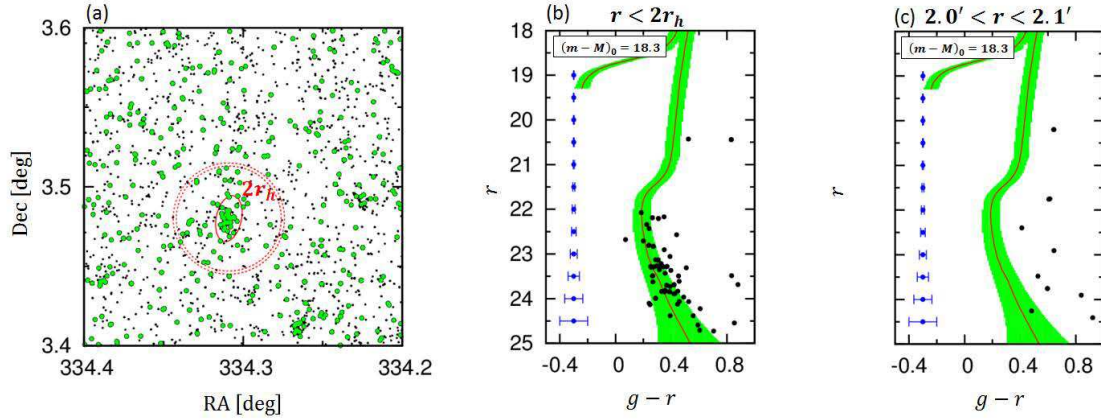


Fig. 8. (a) The spatial distribution of the objects around the overdensity, HSC 1. The green circles and black dots denote, respectively, the objects inside and outside the isochrone filter at $(m - M)_0 = 18.3$. In this plot, all of the objects without taking into account the *extendedness* parameter are shown to avoid the effect of the deblender failure in the star/galaxy separation. A solid red curve shows an ellipse with a major axis of $r = 2r_h$ ($r_h = 0'.44$) and an ellipticity of 0.46, whereas dashed red circles mark an annulus with radii $2'.0$ and $2'.1$ from the center. (b) The CMD of the objects defined in the $g - r$ vs. r CMD relation, which are located within the solid red ellipse in panel (a), where we use the undebled flux of the HSC image with a seeing-matched aperture magnitude to avoid the effect of the deblender failure in this crowded region. (c) The same as (b) but for the objects at $2'.0 < r < 2'.1$ having the same solid angle, i.e., the field objects outside the overdensity. Note the absence of a main sequence feature seen in (b).

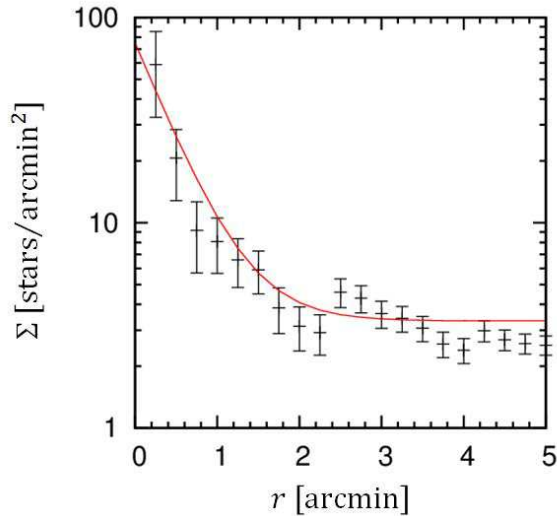


Fig. 9. The density distribution of the stars in HSC 1 passing the isochrone filter given in Figure 8(b), in elliptical annuli as a function of mean radius. The uncertainties are based on Poisson statistics. The red line denotes the best-fit exponential profile with $r_h = 0'.44$.

affect the radial distribution of subhalos at redshift $z = 0$. The first is due to the finite resolution of the simulation, which leads to a number of spatially unresolved subhalos. They made use of a semi-analytical galaxy formation model to account for these otherwise unresolved subhalos (or ‘orphan galaxies’). Second, they considered the effect of subhalo depletion due to tidal interaction with a central baryonic disk (an effect which is not included in this pure DM simulation). These two effects work in opposite senses, and they found that the normalized radial distribution of these fiducial subhalos is well fit to a so-called

Einasto profile (Einasto 1965; Navarro et al. 2004) and is similar to that of luminous satellites obtained from high-resolution hydrodynamic simulations from the project called APOSTLE (Fattahi et al. 2016; Sawala et al. 2016b). For an assumed MW halo mass of $1.0 \times 10^{12} M_\odot$, they find that the total number of satellites with $M_V \leq 0$ within 300 kpc of the Sun is 124^{+40}_{-27} (see their Table E1); this number is only weakly dependent on halo mass. This cumulative luminosity function is denoted as $N(M_V)$ in what follows.

Given this predicted number of visible satellites, we evaluate the HSC-SSP survey area and depth to obtain the actual number of satellites it should be able to detect. First, HSC-SSP in its Wide layer has surveyed over $\sim 676 \text{ deg}^2$, which corresponds to a fraction of the sky, $f_{\Omega, \text{HSC}} = 0.016$. The number of expected satellites over this solid angle is given by $f_{\Omega, \text{HSC}} N(M_V)$.

Second, we evaluate the completeness correction associated with the detection limit of HSC, $f_{r, \text{HSC}}$, which depends on M_V . Following Newton et al. (2018), we assume that the radial distribution of satellites in this case follows an Einasto profile and is independent of their luminosities. With this, $f_{r, \text{HSC}}$ is given by

$$f_{r, \text{HSC}} = \frac{N(< R_{\text{comp}}^{\text{HSC}})}{N(< 300 \text{ kpc})} = \frac{\gamma\left(\frac{3}{\alpha}, \frac{2}{\alpha} \left[c_{200} \frac{R_{\text{comp}}^{\text{HSC}}}{R_{200}} \right]^\alpha\right)}{\gamma\left(\frac{3}{\alpha}, \frac{2}{\alpha} \left[c_{200} \frac{300 \text{ kpc}}{R_{200}} \right]^\alpha\right)}, \quad (4)$$

where γ is the lower incomplete Gamma function, defined as

$$\gamma(s, x) = \int_0^x t^{s-1} \exp(-t) dt. \quad (5)$$

The Einasto profile, $\ln N(r)/N_{-2} = -(2/\alpha)[(r/r_{-2})^\alpha - 1]$, is parameterized by a shape parameter α and the concentration, $c_{200} = R_{200}/r_{-2}$, where r_{-2} denotes the radius at which the logarithmic slope of the profile is -2 and the density there is

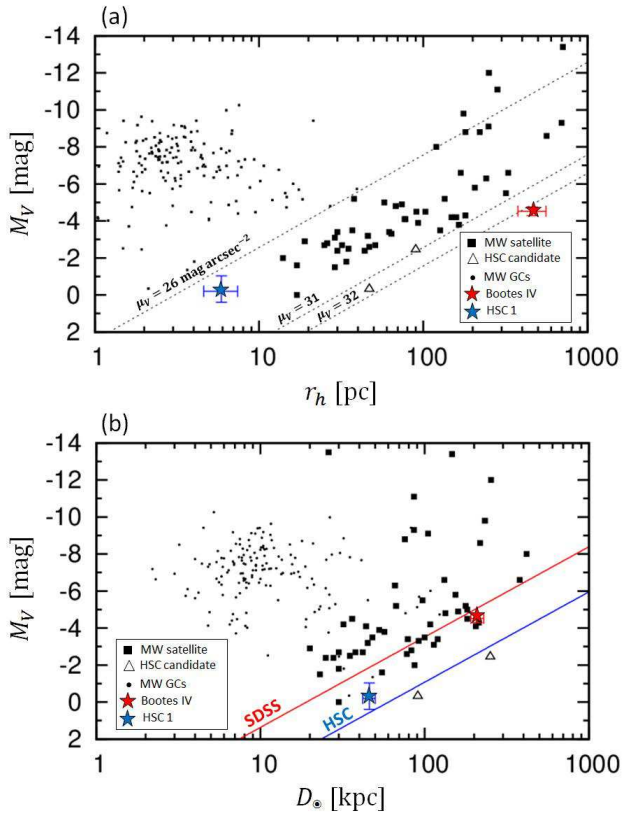


Fig. 10. (a) The relation between M_V and r_h for MW globular clusters (dots) taken from Harris (1996) and MW dSphs (filled squares) from McConnachie (2012); Laevens et al. (2014); Bechtol et al. (2015); Koposov et al. (2015); Drlica-Wagner et al. (2015); Kim et al. (2015); Kim & Jerjen (2015); Laevens et al. (2015a); Laevens et al. (2015b); Torrealba et al. (2016); Torrealba et al. (2018). The empty triangles denote those found from the previous data release of the HSC-SSP (Homma et al. 2016; Homma et al. 2018). The red and blue stars with error bars, respectively, denote Bootes IV and HSC 1. The dotted lines denote the loci of constant surface brightness, $\mu_V = 26, 31,$ and $32 \text{ mag arcsec}^{-2}$. (b) The relation between M_V and heliocentric distance, D_\odot . The red and blue lines denote, respectively, the detection limits of SDSS and HSC.

N_{-2} . We adopt $\alpha = 0.24$, $c_{200} = 4.9$ and $R_{200} = 200 \text{ kpc}$ for a $1.0 \times 10^{12} M_\odot$ MW-sized halo (Newton et al. 2018). The total number of satellites predicted for the current HSC-SSP data, after the combined correction for both of the above effects, is now given as $f_{r,\text{HSC}} f_{\Omega,\text{HSC}} N(M_V)$.

In Figure 11, the black solid line shows the predicted cumulative luminosity function of all the visible satellites from the study of Newton et al. (2018), namely 124^{+40}_{-27} for $M_V \leq 0$. The blue solid line denotes the luminosity function considering the correction for the sky coverage only, $f_{\Omega,\text{HSC}}$, whereas the red solid line includes the full correction, $f_{r,\text{HSC}} f_{\Omega,\text{HSC}}$, i.e., the expected number of visible satellites in the HSC-SSP survey of S18A, given as $1.5^{+0.4}_{-0.3}$ for $M_V \leq 0$. We note that this number is very weakly dependent on the values for (a^*, b^*) in equation (2); varying these over a reasonable range changes this number

by only ~ 0.1 . In addition, Newton et al. (2018) find that the total number of satellites is insensitive to the assumed MW halo mass; varying that mass from 0.5 to $2.0 \times 10^{12} M_\odot$ changes the cumulative number, N , by no more than the 68% uncertainty range indicated above.

The green solid line in Figure 11 corresponds to the cumulative luminosity distribution of the identified satellites within the HSC-SSP footprint of $\sim 676 \text{ deg}^2$. This sample includes six satellites of Sextans ($M_V = -9.3$: classical dwarf), Leo IV ($M_V = -5.8$: SDSS DR9), Pegasus III ($M_V = -3.4$: SDSS DR9), Cetus III ($M_V = -2.4$: HSC), Virgo I ($M_V = -0.3$: HSC) and Bootes IV. That is, we find six dwarf galaxies, whereas the model predicted only $1.5^{+0.4}_{-0.3}$. Thus, we apparently have a problem of too many satellites, instead of a missing satellites problem. We note that the Newton et al. (2018) prediction is normalized with the sample of visible satellites found in SDSS and DES, so it is not sensitive to the information of satellites at much larger distances as those found by the current deeper survey. Also, the larger number of observed satellites may be due to the effect of a massive dwarf galaxy with 10^9 to $10^{10} M_\odot$ as one of main progenitors for the formation of the stellar halo, which merged with the MW around 6 to 10 Gyr ago, as suggested from the kinematics analysis of nearby stars from *Gaia* (e.g., Fattahi et al. 2018; Belokurov et al. 2018; Helmi et al. 2018). If that is the case, then this progenitor would bring additional subhalos and thus visible satellites with it, as suggested from the discovery of UFDs associated with the Magellanic Clouds in the DES survey (Jethwa et al. 2016; Dooley et al. 2017), as first suggested by Lynden-Bell (1976). Also, there may exist some diversity in the luminosity function of satellites in MW-sized host galaxies, as suggested from the recent study of nearby galaxies outside the Local Group (Tanaka et al. 2018), implying that the total population of subhalos is actually sensitive to the characteristics of each MW-sized host halo, including their total mass and merging history. Indeed, if we adopt the abundance matching model by Dooley et al. (2017) as adopted in our previous papers, the predicted number of satellites in the HSC-SSP survey area is estimated as $N = 4^{+8}_{-2}$, i.e., in agreement with the current discovery rate of satellites within a 1σ uncertainty. This may suggest that the models need more refinements for the assignment of dark subhalos to visible satellites.

The answer to this issue is beyond the scope of this work, but will be available as further UFDs are found in the on-going HSC-SSP and the LSST (Abell et al. 2009).

5 Conclusions

From the HSC-SSP data obtained through 2018 April, we have found a highly compelling UFD candidate, Bootes IV, and a globular cluster candidate, HSC 1. These objects were identi-

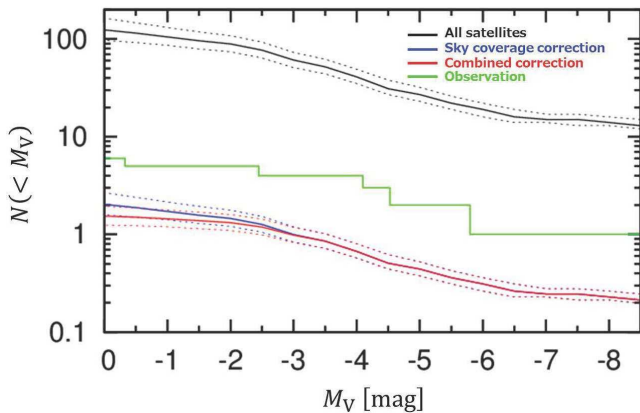


Fig. 11. The black solid line shows the cumulative luminosity distribution of all visible satellites obtained from the study of Newton et al. (2018), namely 124^{+40}_{-27} for $M_V \leq 0$. The blue solid line accounts for the correction related to the sky coverage only, $f_{\Omega, \text{HSC}}$, of the HSC-SSP survey and the red solid line accounts for all the corrections associated with the HSC-SSP survey. Dotted lines above and below each of the black, blue and red solid lines correspond to the 68 % confidence range associated with these estimates. The green solid line corresponds to the observed cumulative luminosity distribution of satellites identified within the HSC-SSP footprint of $\sim 676 \text{ deg}^2$, which consists of Sextans, Leo IV, Pegasus III, Cetus III, Virgo I and Boötes IV.

fied as statistically high overdensities of 32.3σ and 31.8σ , respectively, in the relevant isochrone filter with age of 13 Gyr and metallicity of $[M/H] = -2.2$. Based on a maximum likelihood analysis, the half-light radius of Boötes IV is obtained as $r_h = 462^{+98}_{-84}$ pc and its V-band absolute magnitude is $M_V = -4.53^{+0.23}_{-0.21}$ mag. This follows the size-brightness relation for other MW dwarf satellites, suggesting that it is a dwarf galaxy. For HSC 1, we have obtained $r_h = 5.9^{+1.5}_{-1.3}$ pc and $M_V = -0.20^{+0.59}_{-0.83}$ mag, thus suggesting that it is a globular cluster because its size is comparable with MW globular clusters having the same luminosity, although spectroscopic studies are needed to determine if there is evidence for associated dark matter.

In the $\sim 676 \text{ deg}^2$ covered to date in *gri* in the HSC-SSP footprint, we have identified three new UFDs from the HSC data (Virgo I, Cetus III and Boötes IV) and there exist three previously known satellites. To investigate what this number of satellites implies in view of Λ CDM models, we adopt the recent theoretical estimate of satellite populations in a MW-sized halo by Newton et al. (2018), in which the sample of luminous satellites found in SDSS and DES are considered and a prior for their radial distribution is inferred from the AQUARIUS suite of high-resolution dark-matter only simulations, taking into account both the effects of the unresolved population of subhalos due to finite numerical resolution and their depletion due to tidal forces from the central disk galaxy. This model predicts that HSC should have seen $1.5^{+0.4}_{-0.3}$ satellites with $M_V \leq 0$ within the HSC detection limit, to be compared with the observed number of six. The Newton et al. (2018) prediction is insensitive to the mass of the MW halo and the adopted values for the param-

eters relevant for identifying satellites. However, the fact that we observe more satellites than predicted may be due to the presence of diversity in the total satellite population depending on the characteristics of each MW-sized host halo including their total mass and merging history. For instance, analysis of the *Gaia* sample of nearby stars (Belokurov et al. 2018; Helmi et al. 2018) indicates that a $10^9 - 10^{10} M_{\odot}$ galaxy fell into the MW stellar halo as suggested from their possible debris present in the sample; this Large Magellanic Cloud-class satellite may be associated with additional subhalos as suggested by analyses of the DES survey (Jethwa et al. 2016; Dooley et al. 2017). Another possibility is that the Newton et al. (2018) model is not sensitive to the information of more distant satellites as found by the current deeper survey than SDSS and DES. This suggests that the theoretical models need more refinements for the assignment of dark subhalos to luminous satellites.

Before concluding this, we require spectroscopic follow-up studies of UFDs discovered from the HSC imaging data to constrain their luminosities based on the identification of member stars, as well as their dynamical masses deduced from the velocity distribution of stars. We have already obtained spectra of several of these candidates. The completion of the HSC-SSP survey program will provide a more robust constraint on the observed number of satellites, which will eventually shed light on the nature of dark matter on small scales, i.e. the scales of galaxies and satellites.

Acknowledgments

This work makes use of data collected at the Subaru Telescope and retrieved from the HSC data archive system, which is operated by Subaru Telescope and Astronomy Data Center at National Astronomical Observatory of Japan. MC thanks support from MEXT Grant-in-Aid for Scientific Research on Innovative Areas (No. 15H05889, 16H01086, 18H04334). NA is supported by the Brain Pool Program, which is funded by the Ministry of Science and ICT through the National Research Foundation of Korea (2018H1D3A2000902).

The HSC collaboration includes the astronomical communities of Japan and Taiwan, and Princeton University. The HSC instrumentation and software were developed by the National Astronomical Observatory of Japan (NAOJ), the Kavli Institute for the Physics and Mathematics of the Universe (Kavli IPMU), the University of Tokyo, the High Energy Accelerator Research Organization (KEK), the Academia Sinica Institute for Astronomy and Astrophysics in Taiwan (ASIAA), and Princeton University. Funding was contributed by the FIRST program from Japanese Cabinet Office, the Ministry of Education, Culture, Sports, Science and Technology, the Japan Society for the Promotion of Science, Japan Science and Technology Agency, the Toray Science Foundation, NAOJ, Kavli IPMU, KEK, ASIAA, and Princeton University.

This paper utilizes software developed for the LSST. We thank the LSST Project for making their code freely available at <http://dm.lsst.org>.

The PS1 Surveys have been made possible through contributions of the Institute for Astronomy, the University of Hawaii, the Pan-STARRS Project Office, the Max-Planck Society and its participating in-

stitutes, the Max Planck Institute for Astronomy, Heidelberg and the Max Planck Institute for Extraterrestrial Physics, Garching, The Johns Hopkins University, Durham University, the University of Edinburgh, Queen's University Belfast, the Harvard-Smithsonian Center for Astrophysics, the Las Cumbres Observatory Global Telescope Network Incorporated, the National Central University of Taiwan, the Space Telescope Science Institute, the National Aeronautics and Space Administration under Grant No. NNX08AR22G issued through the Planetary Science Division of the NASA Science Mission Directorate, the National Science Foundation under Grant No. AST-1238877, the University of Maryland, and Eotvos Lorand University and the Los Alamos National Laboratory.

References

- Abazajian, K., Adelman-McCarthy, J. K., Agüeros, M. A., et al. 2004, *AJ*, 128, 502
- Abbott, T., Abdalla, F. B., Allam, S., et al. 2016, *MNRAS*, 460, 1270
- Abell, P. A. et al. 2009, *LSST Science Book*, Version 2.0, arXiv:0912.0201
- Aihara, H., Arimoto, N., Armstrong, R., et al. 2018a, *PASJ*, 70, S4 (HSC overview and survey paper)
- Aihara, H., Armstrong, R., Bickerton, S., et al. 2018b, *PASJ*, 70, S8 (HSC DR1 paper)
- Axelrod, T., Kantor, J., Lupton, R. H., & Pierfederici, F. 2010, in *Proc. SPIE*, Vol. 7740, *Software and Cyberinfrastructure for Astronomy*, 774015
- Bechtol, K., Drlica-Wagner, A., Balbinot, E., et al. *ApJ*, 807, 50
- Belokurov, V., Zucker, D. B., Evans, N. W., et al. 2006, *ApJL*, 647, L11
- Belokurov, V., Erkal, D., Evans, N. W., et al. 2006, *MNRAS*, 478, 611
- Bosch, J., Armstrong, R., Bickerton, S., et al. 2018, *PASJ*, 70, S5
- Boylan-Kolchin, M., Bullock, J. S., Kaplinghat, M. 2011, *MNRAS*, 415, L40
- Boylan-Kolchin, M., Bullock, J. S., Kaplinghat, M. 2012, *MNRAS*, 422, 1203
- Bressan, A., Marigo, P., Girardi, L., et al. 2012, *MNRAS*, 427, 127
- Burkert, A. 1995, *ApJ*, 447, L25
- Chabrier, G., 2001, *ApJ*, 554, 1274
- Chambers, K. C., et al. 2016, arXiv: 1612.05560
- de Blok, W. J. G., McGaugh, S. S., Bosma, A., & Rubin, V. C. 2001, *ApJ*, 552, L23
- Deason, A. J., Belokurov, V., & Evans, N. W. 2011, *MNRAS*, 416, 2903
- Dooley, G. A., Peter, A. H. G., Carlin, J. L. et al. 2017, *MNRAS*, 472, 1060
- Drlica-Wagner, A., Bechtol, K., Rykoff, E. S., et al. 2015, *ApJ*, 813, 109
- Einasto, J. *Trudy Inst. Astroz. Alma-Ata*, 5, 87
- Fattahi, A., Belokurov, V., Deason, A. J. et al. 2018, preprint (arXiv:1810.07779)
- Fattahi, A., et al. 2016, *MNRAS*, 457, 844
- Fukushima, T., Chiba, M., Tanaka, M. et al. 2019, *PASJ*, in press (arXiv:1904.04966)
- Furusawa, H., et al. 2018, *PASJ*, 70, S3
- Garrison-Kimmel, S., Bullock, J. S., Boylan-Kolchin, M., & Bardwell, E. 2017, *MNRAS*, 464, 3108
- Gilmore, G., Wilkinson, M. I., Wyse, R. F. G., et al. 2007, *ApJ*, 663, 948
- Griffen, B. F., Ji, A. P., Dooley, G. A., et al. 2016, *ApJ*, 818, 10
- Gunn, J. E., & Stryker, L. L., 1983, *ApJS*, 52, 121
- Harris, W. E. 1996, *AJ*, 112, 1487
- Helmi, A., Babusiaux, C., Koppelman, H. H. et al. 2018, preprint (arXiv:1806.06038)
- Homma, D., Chiba, M., Okamoto, S., et al. 2016, *ApJ*, 832, 21
- Homma, D., Chiba, M., Okamoto, S., et al. 2018, *PASJ*, 70, S18
- Ibata, R. A., Lewis, G. F., Conn, A. R., et al. 2013, *Nature*, 493, 62
- Ivezić, Z., Axelrod, T., Brandt, W. N., et al. 2008, *AJ*, 176, 1
- Jethwa, P., Erkal, D., Belokurov, V. 2016, *MNRAS*, 461, 2212
- Jordi, K., Grebel, E. K., Ammon, K. 2006, *aj*, 460, 339
- Jurić, M., Kantor, J., Lim, K.-T., et al. 2017, *ASPC*, 512, 279
- Kawanomoto, S. et al. 2018, *PASJ*, 70, 66
- Kim, D., Jerjen, H., Milone, A. P. et al. 2015, *ApJ*, 803, 63
- Kim, D., & Jerjen, H. 2015, *ApJ*, 808, L39
- Klypin, A., Kravtsov, A. V., Valenzuela, O., & Prada, F. 1999, *ApJ*, 522, 82
- Komiyama, Y., et al. 2018, *PASJ*, 70, S2
- Koposov, S., Belokurov, V., Evans, N. W., et al. 2008, *ApJ*, 686, 279
- Koposov, S. E., Belokurov, V., Torrealba, G., & Evans, N. W. 2015, *ApJ*, 805, 130
- Kroupa, P., 2002, *Science*, 295, 82
- Kroupa, P., Theis, C., & Boily, C. M. 2005, *A&A*, 431, 517
- Laevens, B. P. M., Martin, N. F., Sesar, B., et al. 2014, *ApJL*, 786, L3
- Laevens, B. P. M., Martin, N. F., Ibata, R. A. et al. 2015a, *ApJL*, 802, L18
- Laevens, B. P. M., Martin, N. F., Bernard, E. J. et al. 2015b, *ApJL*, 813, L44
- Leauthaud, A., Massey, R., Kneib, J.-P., et al. 2007, *ApJS*, 172, 219
- Lynden-Bell, D. 1976, in *Dickens, R. J., Perry, J. E., Smith, F. G., King, I. R., eds, Royal Greenwich Observatory Bulletins Vol. 182, The Galaxy and the Local Group*. Royal Greenwich Observatory, p. 235
- Macciò, A. V., & Fontanot, F. 2010, *MNRAS*, 404, L16
- Magnier, E. A., Schlafly, E., Finkbeiner, D., et al. 2013, *ApJS*, 205, 20
- Marchi-Lasch, S. et al. 2019, preprint (arXiv:1902.08860)
- Martin, N. F., de Jong, J. T. A., & Rix, H.-W. 2008, *ApJ*, 684, 1075
- Martin, N. F., Ibata, R. A., Lewis, G. F., et al. 2016, *ApJ*, 833, 167
- McConnachie, A. W., & Irwin, M. J. 2006, *MNRAS*, 365, 902
- McConnachie, A. W., 2012, *AJ*, 144, 4
- Milosavljević, M., & Bromm, V. 2014, *MNRAS*, 440, 50
- Miyazaki, S., Komiyama, Y., Nakata, H., et al. 2012, *Proc. SPIE*, 8446, 84460Z
- Miyazaki, S., Komiyama, Y., Kawanomoto, S. et al. 2018, *PASJ*, 70, S1
- Moore, B., 1994, *Nature*, 370, 629
- Moore, B., Ghigna, S., Governato, F., Lake, G., Quinn, T., & Stadel, J. 1999, *ApJL*, 524, L19
- Navarro, J. F. et al. 2004, *MNRAS*, 349, 1039
- Newton, O., Cautun, M., Jenkins, A., et al. 2018, *MNRAS*, 479, 2853
- Oh, S.-H., de Blok, W. J. G., Brinks, E., Walter, F., & Kennicutt, Jr., R. C. 2011, *AJ*, 141, 193
- Okayasu, Y., & Chiba, M. 2016, *ApJ*, 827, 105
- Pawlowski, M. S., Pflamm-Altenburg, J., & Kroupa, P. 2012, *MNRAS*, 423, 1109
- Pawlowski, M. S., Kroupa, P., & Jerjen, H. 2013, *MNRAS*, 435, 1928
- Pawlowski, M. S., Famaey, B., Merritt, D., & Kroupa, P. 2015, *ApJ*, 815, 19
- Sakamoto, T., & Hasegawa, T. 2006, *ApJ*, 653, L29
- Salpeter, E. E. 1955, *ApJ*, 121, 161
- Sawala, T., Frenk, C. S., & Fattahi, A., et al. 2016, *MNRAS*, 457, 1931
- Sawala, T., Frenk, C. S., Fattahi, A., et al. 2016, *MNRAS*, 456, 85
- Schlafly, E. F., & Finkbeiner, D. P. 2011, *ApJ*, 737, 103
- Schlafly, E. F., Finkbeiner, D. P., Jurić, M., et al. 2012, *ApJ*, 756, 158

- Schlegel, D. J., Finkbeiner, D. P., & Davis, M. 1998, *ApJ*, 500, 525
Simon, J. D., & Geha, M. 2007, *ApJ*, 670, 313
Springel, V. et al. 2008, *MNRAS*, 391, 1685
Tanaka, M., Chiba, M., Hayashi, K. et al. 2018, *ApJ*, 865, 125
Tegmark, M. et al., 2004, *ApJ*, 606, 702
Tollerud, E. J., Bullock, J. S., Strigari, L. E., & Willman, B. 2008, *ApJ*, 688, 277
Tonry, J. L., Stubbs, C. W., Lykke, K. R., et al. 2012, *ApJ*, 750, 99
Torrealba, G. et.al. 2016, *MNRAS*, 463, 712
Torrealba, G. et.al. 2018, *MNRAS*, 475, 5085
Walsh, S. M., Willman, B., & Jerjen, H. 2009, *AJ*, 137, 45
Willman, B., Dalcanton, J., Ivezić, Z. et al. 2002, *AJ*, 123, 848
Willman, B., Blanton, M. R., West, A. A., et al. 2005, *AJ*, 129, 2692
York, D. G., Adelman, J., Anderson, J. E., Jr., et al. 2000, *AJ*, 120, 1579